iScience

Article

Metabolic activity grows in human cancers pushed by phenotypic variability

Diagnostic PET images
512 cancer patients

Hotspot of activity (SUV$_\text{max}$)
Metabolic tumor volume (MTV)
Average activity (SUV$_\text{mean}$)

$$\text{SUV}_\text{max} = \alpha\,\text{SUV}_\text{mean}^{\,\beta}$$

$$\text{SUV}_\text{max} = \alpha\,\text{MTV}^{\beta}$$

$\log(\text{SUV}_\text{max})$

$\log(\text{SUV}_\text{mean})$
$\beta \approx 1.2$

$\log(\text{SUV}_\text{max})$

MTV
$\beta \approx 0.3$

Jesús J. Bosque,
Gabriel F. Calvo,
David Molina-García, Julián
Pérez-Beteta, Ana
M. García Vicente,
Víctor M. Pérez-García

jesus.bosque@uclm.es

Highlights

The metabolic hotspot in human cancers becomes more active as tumors grow

Hotspot activity grows faster than the rest of the tumor and promotes heterogeneity

A mathematical model capturing phenotypic transitions reproduces the patient data

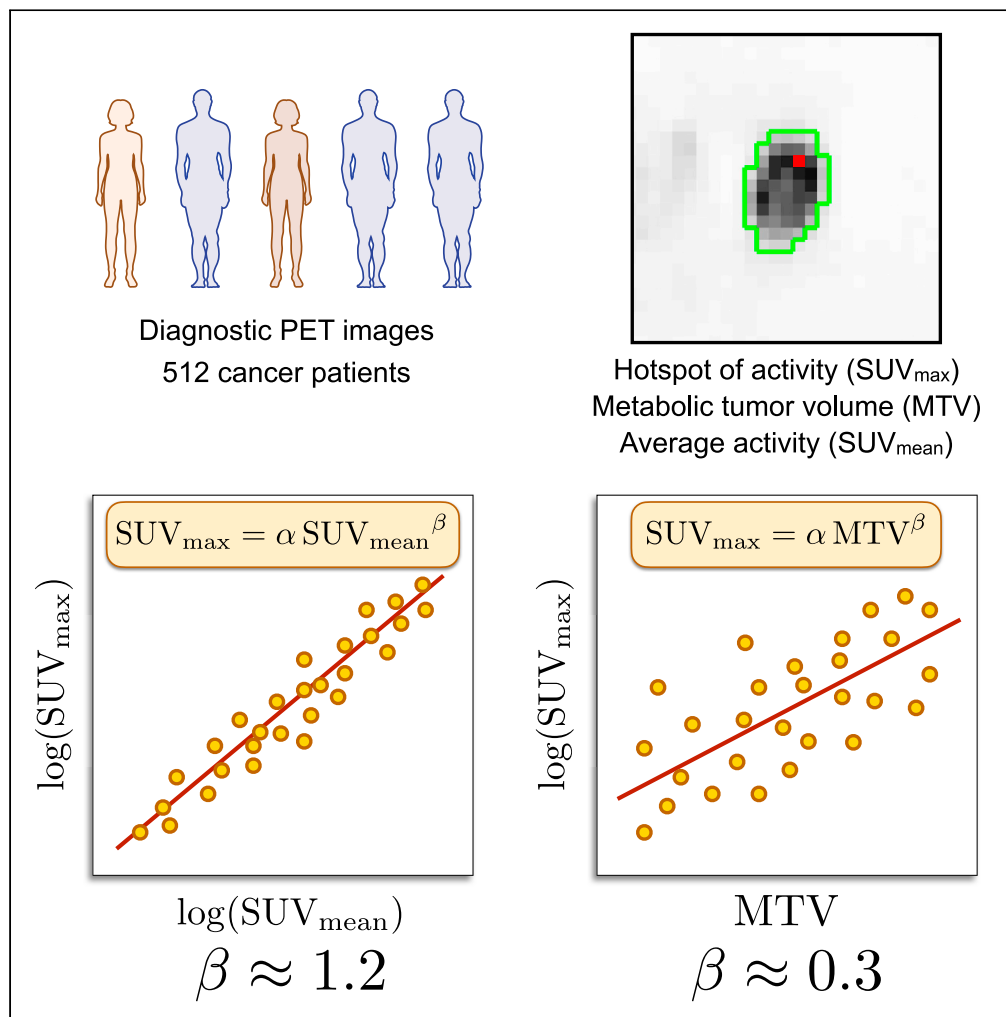Non-genetic changes may suffice to fuel these increases in tumor metabolic activity

Article

Metabolic activity grows in human cancers pushed by phenotypic variability

Jesús J. Bosque,[1,3,*] Gabriel F. Calvo,[1] David Molina-García,[1] Julián Pérez-Beteta,[1] Ana M. García Vicente,[2] and Víctor M. Pérez-García[1]

SUMMARY

Different evolutionary processes push cancers to increasingly aggressive behaviors, energetically sustained by metabolic reprogramming. The collective signature emerging from this transition is macroscopically displayed by positron emission tomography (PET). In fact, the most readily PET measure, the maximum standardized uptake value (SUV_{max}), has been found to have prognostic value in different cancers. However, few works have linked the properties of this metabolic hotspot to cancer evolutionary dynamics. Here, by analyzing diagnostic PET images from 512 patients with cancer, we found that SUV_{max} scales superlinearly with the mean metabolic activity (SUV_{mean}), reflecting a dynamic preferential accumulation of activity on the hotspot. Additionally, SUV_{max} increased with metabolic tumor volume (MTV) following a power law. The behavior from the patients data was accurately captured by a mechanistic evolutionary dynamics model of tumor growth accounting for phenotypic transitions. This suggests that non-genetic changes may suffice to fuel the observed sustained increases in tumor metabolic activity.

INTRODUCTION

The development of cancer involves the accumulation of genetic and epigenetic alterations leading to a broad diversity of subclones that compete for space and resources.[1,2] The evolutionary dynamics resulting from these heterogeneous populations lead to the selection of cells having better fitness, for instance in their proliferation rate, which implies that there is a progression to higher grades of malignancy with time.[3,4] To sustain their energetic requirements imposed by these alterations, tumor cells deploy a repertoire of metabolic adaptations that allow them to thrive under detrimental conditions,[5] being the most common a preference for a glycolytic metabolism and avidity for glucose.[6]

Positron emission tomography (PET) leverages this reprogramming to render a spatially structured three-dimensional image of the tumor metabolic state. The so-called standardized uptake value (SUV) of any biomolecule analog is computed in each voxel to generate a macroscopic visualization that emerges from the collective behavior at the cellular level.[7,8] Accordingly, PET data provides a macroscopic picture of the trajectory followed by cancers to more malignant states. Nevertheless, few studies have taken advantage of this information from an evolutionary dynamics perspective.[9,10] The simplest PET-derived parameter, the activity of the hotspot (SUV_{max}), is now an essential tool in cancer diagnosis and monitoring.[11,12] The SUV_{max} is known to provide relevant prognostic information in many cancers, with higher values being associated with worse outcomes.[13–17] However, the evolutionary dynamics processes underlying its significance have been mostly unexplored.

Mathematical models of cancer dynamics allow us to unveil and quantify the principles that rule progression.[18,19] These have usually focused on genetic instability as the main driver of clonal evolution,[20] even though other mechanisms might be also relevant.[21] The results point to an evolution to states of higher malignancy and faster tumor growth rate, even when the selective advantages can be small.[22] Recent studies have used mechanistic mathematical models to find relevant biomarkers in PET images.[23] Additionally, the application of the scaling laws approach[24,25] to cancer metabolic images has revealed key aspects of how tumors grow.[26] Here, we used mathematical modeling to analyze the evolutionary dynamics behind PET data of patients, and specifically the SUV_{max}.

[1]Department of Mathematics, Mathematical Oncology Laboratory (MOLAB), University of Castilla-La Mancha, Ciudad Real, Spain

[2]Nuclear Medicine Unit, Hospital General Universitario de Ciudad Real, Ciudad Real, Spain

[3]Lead contact

*Correspondence: jesus.bosque@uclm.es

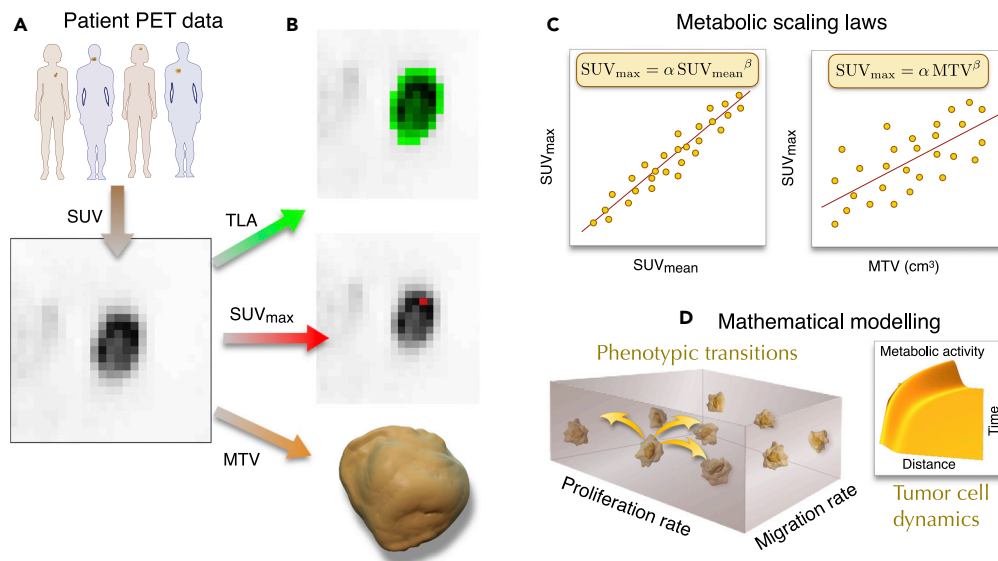https://doi.org/10.1016/j.isci.2023.106118

Figure 1. Overview of the research methodology

(A) PET image acquisition from different patients with cancer and extraction of the standardized uptake value (SUV).

(B) Image analysis and segmentation to obtain the tumor lesion activity (TLA), maximum SUV (SUV_{max}), and metabolic tumor volume (MTV) of each patient.

(C) Regression analysis of each histology to determine the specific metabolic scaling laws between SUV_{max} with both the mean SUV (SUV_{mean}) and the MTV.

(D) Mathematical modeling comprising phenotypic transitions of different tumor cell traits to compute the spatiotemporal dynamics of the metabolic activity.

To understand the increase in cancer aggressiveness during its natural history, we analyzed diagnostic PET images from 512 patients with cancer from six different histologies. Specifically, we focused on a key parameter, SUV_{max}, and its relation to the mean activity in the tumor (SUV_{mean}) together with the metabolic tumor volume (MTV), unveiling the existence of power law relationships. We proposed a mechanistic mathematical model that reproduces the behavior of the patient data. This encompasses cell proliferation, migration, death, and phenotype variability. The formulation, analysis, and results from these models suggest that non-mutational events may suffice to fuel the increase in tumor aggressiveness with time. Figure 1 summarizes the conceptual design of our work.

RESULTS

The activity of the tumor hotspot grows faster than the average activity

We first studied the scaling of SUV_{max} with respect to the SUV_{mean}, which gives an average of the SUV values in the tumor as a whole. We first used four cohorts of patients imaged using ^{18}F-fluorodeoxyglucose (^{18}F-FDG) as a radiotracer (see STAR Methods): lung adenocarcinoma (LUAD), lung squamous cell carcinoma (LUSC), breast cancer (BC), and head and neck cancer (HNC) (Figure 2A). The four cohorts followed power laws ($SUV_{max} = \alpha SUV_{mean}^{\beta}$) with high coefficients of determination ($R^2 > 0.9$, Figure 2B). The β exponents clustered around $\beta \simeq 1.2$ (Figure 2C) and were consistently larger than 1: $\beta = 1.194 \pm 0.023$ (LUAD), $\beta = 1.188 \pm 0.030$ (LUSC), $\beta = 1.155 \pm 0.035$ (BC), and $\beta = 1.173 \pm 0.043$ (HNC).

Two additional cohorts of patients with cancer underwent a PET imaging procedure on diagnosis, using radiotracers that are surrogates for membrane synthesis or, equivalently, cell proliferation: patients with breast cancer (BC-FLT) and patients with glioma (GLI) (Figure 2A). The first group was studied using 3′-deoxy-3′-^{18}F-fluorothymidine (^{18}F-FLT) and the second was imaged with ^{18}F-fluorocholine (^{18}F-FCHOL). Both datasets showed a good fit to a power law, with $R^2 = 0.934$ (BC-FLT) and $R^2 = 0.801$ (GLI). The scaling exponent for BC-FLT was in line with previous results $\beta = 1.206 \pm 0.037$ pointing out that this value might be characteristic of many malignancies. For the GLI cohort, we found a lower coefficient of determination, $R^2 = 0.801$ (Figure 2B) and a substantially smaller scaling exponent $\beta = 1.023 \pm 0.067$ (Figure 2C).
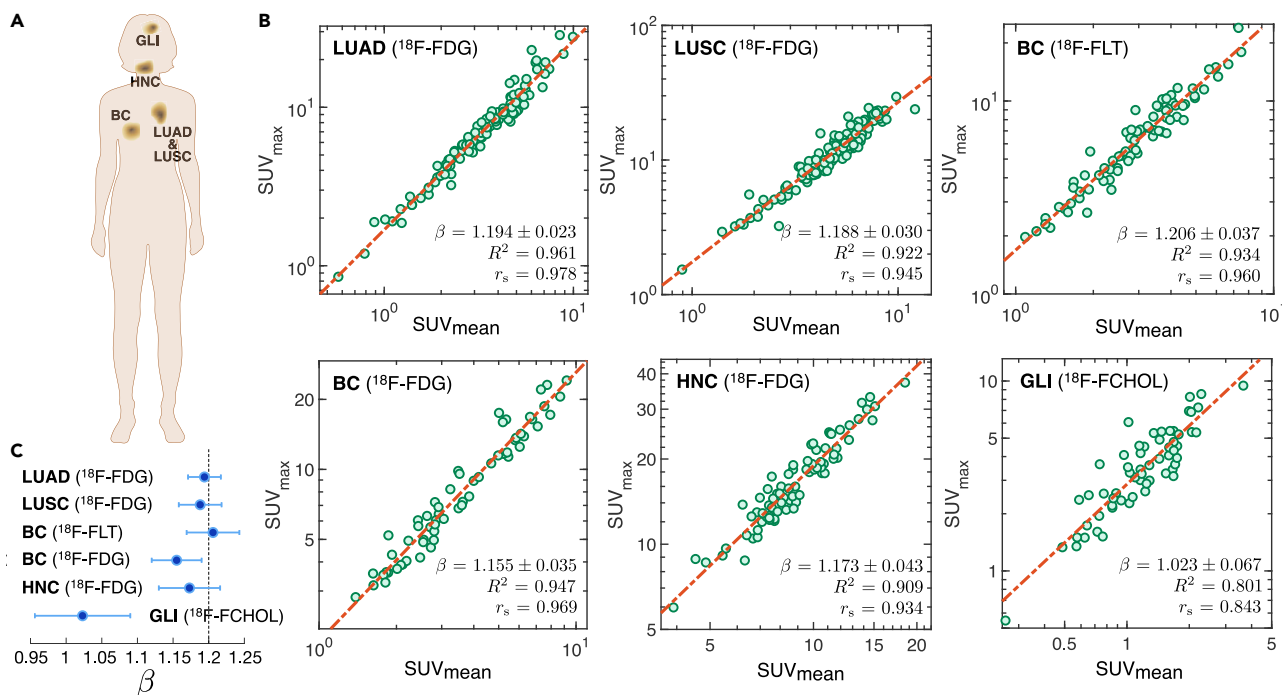
Figure 2. SUV$_{max}$ versus SUV$_{mean}$ from diagnostic PET images of six patients with cancer cohorts

(A) Anatomic location of the different tumors analyzed.

(B) Log-log plots of SUV$_{max}$ versus SUV$_{mean}$ for lung adenocarcinomas (LUAD), lung squamous cell carcinomas (LUSC), breast cancers (BC) and head and neck cancers (HNC), all imaged with ^{18}F-FDG radiotracer (first two columns); breast cancers (BC-FLT) imaged with ^{18}F-FLT and gliomas (GLI) imaged with ^{18}F-FCHOL. All the cohorts were fit to a power law SUV$_{max}$ = αSUV$_{mean}^{\beta}$, plotted by a red dashed line. For each subplot, we show the best scaling exponent β, the coefficient of determination R^2 of the regression, and the Spearman's rank correlation coefficient r_s between both variables.

(C) Summary of the scaling exponents for SUV$_{max}$ versus SUV$_{mean}$ in the six cohorts of patients. The dashed line marks the value β = 1.2.

Maximum tumor activity grows with tumor size for a broad variety of cancers

We then investigated whether the value of SUV$_{max}$ might also follow a power law of the form SUV$_{max}$ = αMTV$^{\beta}$. The exponents found for the different patient cohorts took values in the range [0.217, 0.347], specifically β = 0.305$\pm$0.052 (LUAD), β = 0.217$\pm$0.032 (LUSC), β = 0.347$\pm$0.075 (BC), β = 0.230$\pm$0.036 (HNC), β = 0.257$\pm$0.036 (BC-FLT), β = 0.223$\pm$0.101 (GLI) (Figure 3A). Even though the coefficients of determination were consistently smaller than in the previous SUV$_{max}$-SUV$_{mean}$ relation shown in Figure 2, indicating a lower accuracy of the power law fit, they still reflected an increase of the maximum metabolic activity with volume. The scaling exponents obtained for different cohorts were clustered around the value β = 0.3 (Figure 3B).

Thus our first two key observations were that: **(i)** the maximum tumor activity grew faster than the mean activity value indicating an increased metabolic heterogeneity and **(ii)** the maximum tumor metabolic activity increased with size, pointing out to an increase of tumor aggressiveness during the tumor's natural histories. These results, obtained for different cancer histologies, are in line with the observed correlations between size and aggressiveness for many cancers.

Phenotype variability gives rise to a persistent increase in proliferation activity

We used the EvoFK model (see Box 1) to reproduce *in silico* the spatiotemporal dynamics of metabolic heterogeneity. Low cell density distributions with spherical symmetry and a narrow proliferation width were used as initial data to obtain the radially distributed cell density $n(r, t)$ and metabolic activity $\mathcal{A}(r, t)$ (see STAR Methods for details). Figure 4A plots time snapshots for the cell density spatial profiles. In the early stages, cells are concentrated near the origin, and the density increases in that vicinity. As the tumor progress, cell migration increases leading to a broadening of $n(r, t)$. When the cell density reaches the carrying capacity ($n(r, t)/K$ = 1), the profile adopts the form of a traveling wave that moves as an invading front. Activity profiles are also shown at the same time points in Figure 4A. Initially, most of the proliferative activity occurs at the tumor center. Then, this proliferative profile lifts and occupies a larger space around the
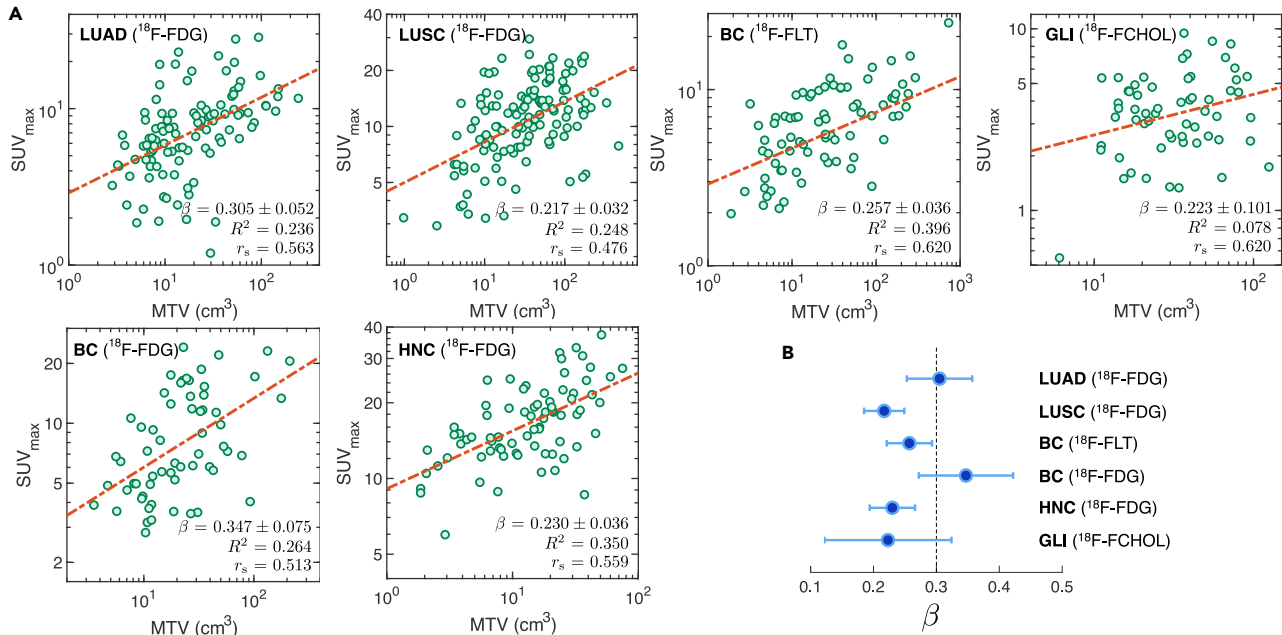
Figure 3. SUV$_{max}$ versus MTV from diagnostic PET images of six different cohorts of patients with cancer

(A) Lung adenocarcinomas (LUAD), lung squamous cell carcinomas (LUSC), breast cancers (BC) and head and neck cancers (HNC), respectively, all imaged with ^{18}F-FDG radiotracer. Breast cancers (BC-FLT) imaged with FLT and gliomas (GLI) imaged with ^{18}F-FCHOL. All the cohorts were fit to a power law SUV$_{max}$ = αMTV$^{\beta}$ plotted by a dashed red line. The fitting exponents that yielded the best β in each case, together with the coefficients of determination R^2 of the regression, and the Spearman's rank correlation coefficient r_s between both variables, are shown in each panel.

(B) Scaling exponent distribution of the power law fits for SUV$_{max}$ versus MTV from diagnostic PET images in the six cohorts of patients cluster around β = 0.3.

lesion core. Eventually, the proliferative profile detaches from the location of the maximum cell density and develops a peak that moves away from the tumor center. This entails that the most proliferative point ceases to be located at the tumor core, even though proliferation might still be large there. Subsequently, the hotspot of $\mathcal{A}(r, t)$ moves toward the tumor boundary (which corresponds to the region where the spatial gradient of the cell density is larger). Moreover, the maximum value of the proliferation activity increases with time as the tumor progress. This parallels the situation of higher activity hotspots with larger MTVs observed in our data.

To further elucidate the contribution of evolutionary dynamics to the growth in tumor activity, we investigated the profiles in the distribution of the proliferation rate. The mechanism of phenotypic variation in Equation 1 is purely stochastic and assumes an equal probability of cells transitioning to a higher/lower proliferative state. At each time step, we calculated the distribution of the proliferation rates for the entire cell population, denoted as $P(\rho, t)$, which represents the probability density function for any cell to have a proliferation rate ρ at a time t (see STAR Methods). Figure 4B displays the time evolution of $P(\rho, t)$ at different time points. Two effects are readily noticeable; a broadening in the phenotype landscape together with a drift in the mode of $P(\rho, t)$ toward higher proliferation values. The first effect contributes to cell heterogeneity, while the second effect reflects the arrow of evolutionary dynamics, evidencing the selection of more aggressive phenotypes. To study the spatial location of more aggressive phenotypes, we calculated the average proliferation rate $\bar{\rho}(r, t)$ as a function of the distance r (inset of Figure 4B). Initially, the average proliferation rate was homogeneously distributed across space but, as the tumor grew, it acquired a sigmoidal shape whose most prominent values occur far from the tumor center.

Hence, the EvoFK model (1) predicts that the presence of fluctuations in the proliferation phenotype, embodied in the diffusion constant D_ρ, leads to an increase with time in the most prominent value of the activity. A noteworthy consequence of this feature is that it captures an internal temporal scale in the evolutionary dynamics of tumor growth. We further explored these results using different values of the diffusion parameters, specifically the pairs $D_c = 3.8 \times 10^{-4}$ cm^2 day^{-1}, $D_\rho = 1.6 \times 10^{-8}$ day^{-3} (Figures S1A and S1B) and $D_c = 4 \times 10^{-5}$ cm^2 day^{-1}, $D_\rho = 1.6 \times 10^{-8}$ day^{-3} (Figures S1C and S1D) with a similar overall behavior.

Box 1. *In silico* spatio-temporal model of tumor phenotypic variability

To connect our observations with evolutionary dynamics processes, we developed a simple conceptual mathematical model (hereinafter denoted EvoFK) based on a continuous Fisher-Kolmogorov-type partial differential equation (PDE) and incorporating cell migration, proliferation, and phenotypic transitions.[21,23] The tumor cell density is assumed to be a function of space $\mathbf{x} \in \Omega \subset \mathbb{R}^3$, and proliferation rate $\rho \in [0, \rho_m]$, where ρ_m is the maximum proliferation rate. A cell density function $u = u(\mathbf{x}, \rho, t)$ encompasses position and proliferation, so that $u(\mathbf{x}, \rho, t)$ represents the density of tumor cells that, at time t, have a proliferation rate ρ at point $\mathbf{x}$. The PDE that models the evolution of the cell density function is

$$\frac{\partial u}{\partial t} = D_c \nabla^2 u + D_\rho \frac{\partial^2 u}{\partial \rho^2} + (\rho - \mu)\left(1 - \frac{1}{K}\int_0^{\rho_m} u(\mathbf{x}, \rho', t)\, d\rho'\right) u. \qquad \text{(Equation 1)}$$

Equation 1 accounts for migration (diffusive motion with motility coefficient $D_c > 0$), phenotypic transitions, and proliferation. The fluctuations in the proliferation phenotype, which occur through a random walk-like process in ρ with diffusion constant $D_\rho > 0$, reflect continuous transitions that change the cell proliferation rate ρ. The third term consists of two mechanisms. The first one includes the proliferation rate ρ minus a constant $\mu > 0$ that regulates the death rate so that those cells having a larger factor $\rho - \mu$ will feature a fitness advantage. The second factor, which has a non-local logistic form (integral over the proliferation variable ρ') with a local carrying capacity $K > 0$, represents the interplay between clones with different phenotypes competing for the available space. Once the function $u = u(\mathbf{x}, \rho, t)$ is computed, the total spatial cell distribution $n(\mathbf{x}, t)$, the proliferation activity $\mathcal{A}(\mathbf{x}, t)$, and other relevant quantities can be defined as described in STAR Methods.

In silico dynamics of SUV$_{max}$ with SUV$_{mean}$ and metabolic tumor volume

To assess *in silico* the changes with time experienced by the activity of the hotspot with respect to the metabolic activity of the overall tumor, we computed the relationship between the maximum value of the activity $\mathcal{A}_{max}(t)$ and the mean activity $\mathcal{A}_{mean}(t)$ (see STAR Methods for their mathematical definitions). The pair $\mathcal{A}_{max}(t) - \mathcal{A}_{mean}(t)$ is depicted in a log-log plot in Figure 4C. The figure shows that the activity in the hotspot grows faster with time than the average tumor activity. Different growth stages are also revealed there. We found that, in the last stage of the simulated time, $\mathcal{A}_{max}(t)$ and $\mathcal{A}_{mean}(t)$ were related by a power law plotted as an orange dashed line in Figure 4C. The slope of the line, corresponding to the exponent of this power law, was $\beta = 1.44$. We also calculated the metabolic tumor volume MTV (t) by selecting the regions of the *in silico* tumor that have a proliferation activity higher than a given threshold $\mathcal{A}_{th}$. Figure 4D depicts the log-log plot pair $\mathcal{A}_{max}(t) - \text{MTV}(t)$ for the same time points. As the metabolically active region of the tumor became larger, the activity hotspot showed a higher maximum. Moreover, from a certain point during the progression, the evolution of $\log(\mathcal{A}_{max}(t)) - \log(\text{MTV}(t))$ became convex, showing an increasingly growing slope. At the last third of the simulated temporal frame of this plot, a power law was fit yielding an exponent $\beta = 0.265$ (slope of the dashed line in Figure 4D). Hence, the results obtained from the time evolution of EvoFK model (1) in the clinically relevant regime were consistent with the scaling laws observed in the datasets.

Full patient cohort simulations replicate the SUV$_{max}$ vs SUV$_{mean}$ and SUV$_{max}$ vs metabolic tumor volume scaling laws

To further substantiate the predictions based on model (1) from Box 1, we generated a synthetic cohort of 150 patients with randomly chosen parameters as described in STAR Methods. For each virtual patient, we computed the MTV (t_{diag}) at the resulting diagnosis time t_{diag}, randomly chosen to replicate the real situation in which patients receive their diagnosis after the tumors have grown without treatment. We also calculated the total lesion activity TLA (t_{diag}). We plotted the pair TLA-MTV for each simulation in Figure 5C and found a scaling law with exponent $\beta = 1.188 \pm 0.013$. Therefore, multiple simulations of the EvoFK model (1) led to results compatible with the observations in patient data[26] (see also Figure S2).

Next, we calculated the maximum activity $\mathcal{A}_{max}(t_{diag})$ and the mean proliferation activity $\mathcal{A}_{mean}(t_{diag})$, both at diagnosis. The log-log plot of the results is shown in Figure 5A. The distribution of these simulations is compatible with a power law having an exponent $\beta = 1.317 \pm 0.009$, which is close to the values obtained for real patients.

We also computed the scaling relations between $\mathcal{A}_{max}(t_{diag})$ and MTV (t_{diag}). A power law with exponent $\beta = 0.259 \pm 0.016$ was obtained. Our simulated data (Figure 5B) reproduced the trend observed in the
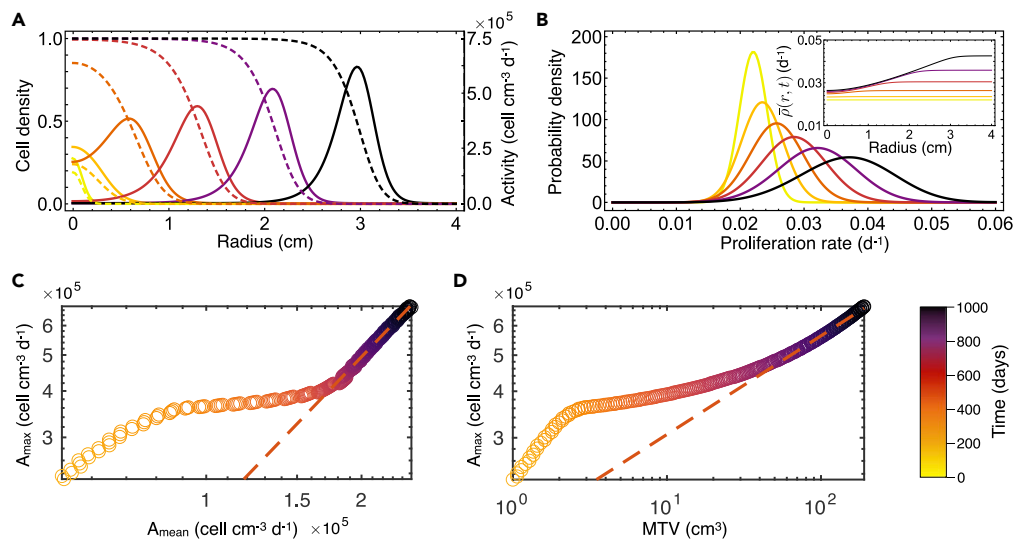
Figure 4. Dynamics of cell density and proliferation activity from simulations of model (1) (Box 1)

(A) Evolution of the cell density normalized to the carrying capacity $n(r, t_j)/K$ (dashed curves) and the corresponding proliferation activity $\mathcal{A}(r, t_j)$ (solid curves) at time points $t_j = 0, 200, 400, 600, 800,$ and 1000 days. The tumor center is located at $r = 0$.

(B) Evolution of the probability density of proliferation rates in the tumor population. The inset shows the spatial profile of the averaged proliferation $\bar{p}(r, t_j)$. Both sets of curves correspond to the same time points as in (A).

(C) Log-log plot of the relation of A_{max} and A_{mean} at each time of the simulation run. The dashed orange line, which has a slope of 1.44, displays the tendency of the circles for sufficiently long times.

(D) Log-log plot of the maximum activity in the tumor A_{max} versus MTV. The dashed orange line, which has a slope of 0.265, displays the tendencies of the simulation data for sufficiently long times. The color code bar denotes the temporal frame of all plots in (A-D). Simulation parameters are listed in STAR Methods. See also Figure S1 for simulations with different values of D_c and D_p.

patient datasets (see Figure 3). Interestingly, not only the obtained exponents were similar in real and simulated data, but also the calculated dispersion is similar in both sets.

To evaluate the dependence of the results on the chosen diffusion parameters, we performed additional sets of simulations of Equation 1 simulating the dynamics of other 1650 virtual patients. These were done in groups of 150, resembling the previous method, but in this case, the parameters were changed. First, we allowed the parameter D_c to be fixed and run simulations with variable D_p for three different values of D_c (Figure S3). Secondly, we allowed D_c to change in our *in silico*-generated cohorts, now with a fixed D_p, and performed three different sets of simulations for fixed values of it (Figure S4). Afterward, we used two different fixed values for the carrying capacity K (Figure S5). Finally, we tested three variations of fixed values of the parameter modulating the death rate μ (Figure S6). Even though the concrete values of the exponents changed within a reasonable range, we found that the conclusions held true for ample ranges of the parameters.

DISCUSSION

Deregulated pathways in cancer lead to unconstrained growth in which genomic instability opens the genomic landscape by enabling successive mutations.[27] After the inactivation of stability genes, mutations in ordinary genes become much more frequent, benefiting tumor progression by producing cell variants with potentially increased fitness.[28] Thus, cancer cells experience a process of clonal evolution[29] allowing them to obtain advantageous traits that fuel their proliferative and invasive potential and are responsible for the progressive increases in tumors' malignancy.[30]

These evolutionary dynamics have a macroscopic reflection in metabolic imaging,[31] in which the hotspot of activity has a special relevance capturing the dynamics of the underlying biology.[23,32,33] For that reason, in this work, we investigated its scaling in relation to the overall uptake of the tumor. In six cohorts of cancer diagnostic PET images, the value of SUV_{max} was related to the SUV_{mean} by a power law with a high coefficient of determination and, in five of the six cohorts, the power-law exponents clustered around $\beta = 1.2$.
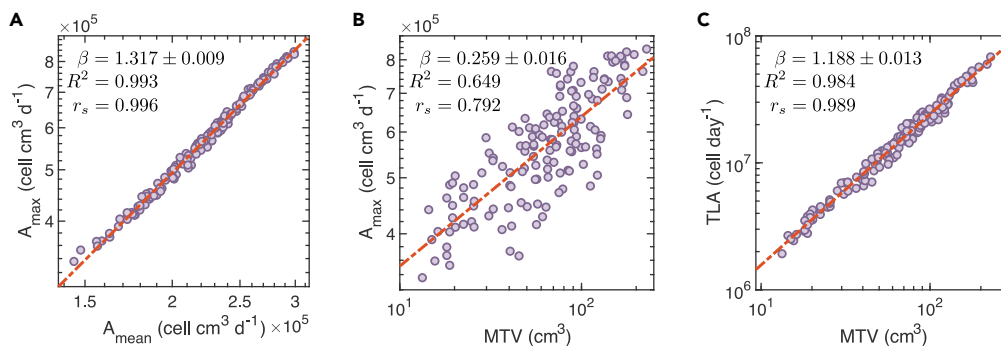
Figure 5. *In silico* scaling laws obtained from numerical simulations of model (1) (Box 1)

(A) Log-log plot of maximum proliferation activity $\mathcal{A}_{max}$ versus mean activity $\mathcal{A}_{mean}$ taken from the final time points of 150 simulations with different values of the main parameters. The dashed line is the result of fitting the data to a power law which gives an exponent of $\beta = 1.317 \pm 0.009$ ($R^2 = 0.993$).

(B) $\mathcal{A}_{max}$ against the metabolic volume MTV follows the tendency of a power law with exponent $\beta = 0.259 \pm 0.016$ ($R^2 = 0.649$).

(C) TLA versus MTV fits with a power law having exponent $\beta = 1.188 \pm 0.013$ ($R^2 = 0.984$). (A-C) In all the cases, the scaling laws between the key variables from the simulations reproduce well what is seen in real data from patients. See Figures S3-S6 for results obtained with different values of the parameters. See Figures 2, 3, and S2 to compare with the corresponding relationships extracted from patients with cancer.

The emergence of these two properties is remarkable and suggests that fundamental principles are at play. Previous works have pointed out that the metabolic activity increases faster than volumetric change,[26] which is also confirmed in this work (Figure S2). Here, the scaling exponents around 1.2 imply that as the total activity of a tumor rises globally, the activity in the SUV_{max} increases faster than the mean: it is the growth in the activity of the SUV_{max} that takes the lead over the global increase in tumor activity. The difference arises in gliomas, where the exponent was very close to 1, pointing to an evolution of the SUV_{max} proportional to the SUV_{mean}. This discrepancy may come from the fact that gliomas are diagnosed at late stages where the hotspot would not have any margin of departure from the whole tumor; there might be a limit in the growth of the activity that is reached at late stages of the tumor evolution. This is in line with works in which low-grade gliomas show an increase in proliferation after therapy, but high-grade gliomas do not.[34]

To gain more insight on the increase of SUV_{max} with time, longitudinal measurements at different time points would be needed, but this type of data is scarce; growing tumors are usually treated or—as in the case of palliative care patients—not followed up with imaging. Since tumor volumes grow during their unperturbed natural evolution, the strategy followed here was comparing the SUV_{max} of different patients with their corresponding MTVs. Even though this approach will be affected by noise, since the comparison is carried out on different patients with independent evolutions, it provides an averaged picture of how both quantities are related. Our results from this perspective revealed a power law relating the SUV_{max} with the MTV, but now with a lower coefficient of determination, as was expected—especially in gliomas, where the R^2 was very low. The low values of R^2 indicate that the power law is not able to model much of the variability in the relationship between both variables, which is in part due to noise—as reflected by the simulations—, nevertheless, the results show a clear tendency of SUV_{max} to be higher for higher MTV. All of the six different cancer cohorts available for our study showed a scaling exponent $\beta \sim 0.3$, reflecting a trend in how the SUV_{max} increases with MTV.

Those results arose with three different radiotracers, two of membrane biosynthesis (^{18}F-FCHOL and ^{18}F-FLT[35,36]) and one of the glucose uptakes (^{18}F-FDG). To support an ever-increasing rate of growth and proliferation, tumors must rearrange their cellular metabolism, which is achieved in part by alterations in the genetic code.[31] This allows them to redirect essential nutrients to the generation of cellular building blocks. It has been longly known that, even in the presence of oxygen, cancer cells process glucose to lactate (aerobic glycolysis) instead of using the mitochondria to oxidize pyruvate to carbon dioxide (oxidative phosphorylation), a pathway that is much more efficient in terms of ATP production. This is joined to a remarkable rise in glucose uptake. Both effects are aimed at optimizing macromolecular biosynthesis to sustain the growth requirements.[37] Thus, glucose is mostly used by tumors for biosynthesis, the reason for which we related the measured activity of the radiotracers to cellular proliferation. Analyzing the

simulations of tumor growth using the EvoFK model (1), and obtaining the proliferation activity through Equation 12, we reproduced computationally the relationships and approximate exponents between TLA and MTV, SUV_{max} and SUV_{mean}, SUV_{max} and MTV, as well as the weak correlation between the later quantities.

Genome instability in cancer expresses preferentially by chromosomal instability (CIN)[38,39] with the loss or acquisition of whole chromosomes and structural aberrations rearranging the location of the genetic material.[40] The accumulation of mutations allows cells to explore the fitness landscape[41] which increases tumor growth rate, tumor grade, and invasiveness.[41,42] Additionally, non-genetic mechanisms such as methylation, acetylation, or chromatin remodeling also affect individual fitness and have to be taken into account.[43,44] Some of those changes are heritable, for what they can enable evolutionary processes,[45,46] and their stochastic nature may affect traits like the proliferative potential driving cell fitnesses and progression.[47,48] Thus the inherent noise in biological systems, and not only the coding mechanisms, contribute to phenotypic variability[49] and has evolutionary consequences.[50] Indeed, random fluctuations are known to have a role in the evolution of different traits including growth rates, affecting the fitness of subgroups of cells in the absence of genetic differences. Some examples have been described in yeast[51] and bacteria.[52]

Our mathematical model was built on the basis of these stochastic epigenetic changes and taking the proliferation rate as the affected variable, modeled by a *continuous* variable subject to a small level of random variability. This is opposed to discrete substantial changes more akin to genetic mutations. Importantly, phenotype changes can go upwards or downwards in aggressiveness with equal probability, however, the emerging evolutionary dynamics drive the tumor to higher proliferative states. This kind of approach, which brings epigenetic modifications into focus, has been well studied in mathematical oncology through a family of models known as phenotype-structured PDE models.[53,54] These typically quantify one or two abstract levels of expression ranging from 0 to 1 which have an impact on a continuous range of phenotypes showing different behavior or response to treatment.[55] With a few exceptions,[56] these models have not traditionally considered the spatial effects of tumor growth explicitly. Here, we joined the phenotype-structured methodology with the classic Fisher-Kolmogorov model to obtain a general model for spatial tumor growth. Moreover, we structured our population by means of an intrinsic trait of the cells, namely, their proliferation rate, which allows us to formulate the model with no additional indefinite attributes. The formulation of the model involves the use of a parameter D_ρ for the variability in the phenotypic changes affecting the proliferation. This parameter has not yet been studied experimentally in humans, although a combination of *in vitro* experiments and analysis of real-time growth of non-small-cell lung carcinoma cells was carried out in ref. [57] and values for D_ρ were estimated. The found values in that work were larger than the ones employed here because our model is applied to patients, for which we expect a slower global dynamics than for the mentioned *in vitro* measurements. With the chosen range of parameters, we predict an evolution of the in silico patients that matches the one observed for the real patients. This range should be understood as a first approximation to the order of this model parameter, although caution must be taken until further experimental methods confirm this.

It is interesting that such a simple model accounting only for a single aspect of evolutionary dynamics can reproduce so well a plethora of the traits identified in metabolic images from real patients. We suggest that the kind of biological effects discussed may have a role in the evolution of the disease, as hinted by the striking similarity between the mathematical model adequacy of our model to the data. Recent research works have provided parallel results in the context of other biological systems.[58] Also, previous mathematical modeling studies in substantially simpler scenarios describing growth *in vitro* have also highlighted the potential role of proliferation fluctuations in the increase of tumor aggressiveness.[57] Here we study the adaptation of the model to data from patients. A joint effort from modelers and clinicians led us to gather diagnostic PET images from six different cohorts of patients with cancer. It would be interesting to broaden the usage of this model to more kinds of cancers, and also to test the behavior in cancers undergoing different treatments. Hopefully, this study will encourage other researchers to test the results found in these cohorts, and extend the conclusions to improve our general knowledge of this group of diseases.

Nevertheless, our model does not intend to be conclusive. Many other attributes such as metastatic/invasive or angiogenic potentials, chemotactic migration,[59] traits conferring resistance to therapies, the levels of oxygen in the microenvironment,[60] the influence of the immune system,[61] and so forth, play a relevant role in the evolutionary dynamics of cancer. It is thus intriguing that a mathematical model including a

limited number of biological phenomena can reproduce the global features of the relationships between the most relevant macroscopic metabolic variables so accurately. This fact may point out either to a dominant role of proliferation as the most relevant trait in the cancers studied and/or an averaging of the potential relevance of other traits at the scale of our observations with voxels of several mm^3 in size.

In conclusion, we have provided evidence from large cohorts of patients with cancer that the metabolic activity increases as the tumors grow, and that this rise is manifestly higher for the most active point of the tumor with respect to its mean activity. To provide a mechanistic explanation for the observations, we have employed a spatiotemporal model of tumor growth that incorporates random changes in a continuous fashion for the proliferation rate. This is inspired by recent experiments and assumes a stochastic and heritable variation in the traits of genetically identical cells. The results from our model in terms of proliferation activity closely resemble traits that are seen in PET images, suggesting that these non-genetic mechanisms may play a role in cancer evolutionary dynamics.

Limitations of the study

To further validate the predictions of the mathematical model used in the present study (see Box 1) in terms of the time evolution of tumor activity, it would be necessary to incorporate longitudinal imaging datasets from different untreated patient cohorts. Data of this type are scarce because growing tumors are typically either treated or—as in the case of palliative care patients—not followed up with imaging. Therefore, in this work, we resort to the use of data from different patients at the time of diagnosis, which inevitably introduces noise to the relationships between variables. Moreover, we used data from six different cohorts of patients with cancer, but it would be advisable to broaden the scope to more types of cancers. It is important to stress that we did not intend to use our mathematical model to make specific predictions of the local dynamics of particular tumors by predicting the local SUV values from the initial data. The model was intended only as a simulation tool allowing us to study *in silico* the interplay between the selected features in untreated tumors: cell motility, proliferation with evolutionary capabilities, cell death, and local competition for space and resources. Possible extensions of the mathematical modeling approach could include allowing variations in the diffusive coefficient to account for evolutionary dynamics effects in cell motility, the interaction with the microenvironment, and so forth.

STAR★METHODS

Detailed methods are provided in the online version of this paper and include the following:

- KEY RESOURCES TABLE
- RESOURCE AVAILABILITY
  - Lead contact
  - Materials availability
  - Data and code availability
- EXPERIMENTAL MODEL AND SUBJECT DETAILS
  - Lung cancer patients (LUAD & LUSC)
  - Breast cancer patients (BC)
  - Head and neck cancer patients (HNC)
  - Breast cancer patients (BC-FLT)
  - Glioma patients (GLI)
- METHOD DETAILS
  - PET image analysis
  - Scaling laws
  - Numerical solution of the PDE model
  - Definition of the key quantities from the model
  - Generation of synthetic patient cohorts
- QUANTIFICATION AND STATISTICAL ANALYSIS
  - Statistical analysis of power law regressions and Spearman's rank correlation

SUPPLEMENTAL INFORMATION

Supplemental information can be found online at https://doi.org/10.1016/j.isci.2023.106118.

AUTHOR CONTRIBUTIONS

Model development and simulation, J.J.B., and G.F.C.; conceptualization, J.J.B., G.F.C., and V.M.P.-G; formal analysis, J.J.B., G.F.C., D.M.-G., and V.M.P.-G; data acquisition, V.M.P.-G., J.P.-B., and A.M.G.V.; data curation, J.J.B., J.P.-B., D.M.-G., V.M.P.-G., and A.M.G.V.; image analysis, J.J.B., J.P.-B., A.M.G.V., and V.M.P.-G.; writing – original draft, J.J.B., G.F.C., and V.M.P.-G.; writing – review and editing, all authors; supervision, G.F.C. and V.M.P.-G.

DECLARATION OF INTERESTS

The authors declare no competing interests.

REFERENCES

1. Turajlic, S., Sottoriva, A., Graham, T., and Swanton, C. (2019). Resolving genetic heterogeneity in cancer. Nat. Rev. Genet. *20*, 404–416.

2. Black, J.R.M., and McGranahan, N. (2021). Genetic and non-genetic clonal diversity in cancer evolution. Nat. Rev. Cancer *21*, 379–392.

3. Williams, M.J., Werner, B., Heide, T., Curtis, C., Barnes, C.P., Sottoriva, A., and Graham, T.A. (2018). Quantification of subclonal selection in cancer from bulk sequencing data. Nat. Genet. *50*, 895–903.

4. Edwards, J., Marusyk, A., and Basanta, D. (2021). Selection-driven tumor evolution with public goods leads to patterns of clonal expansion consistent with neutral growth. iScience *24*, 101901.

5. Faubert, B., Solmonson, A., and DeBerardinis, R.J. (2020). Metabolic reprogramming and cancer progression. Science *368*, eaaw5473.

6. Vander Heiden, M.G., and DeBerardinis, R.J. (2017). Understanding the intersections between metabolism and cancer biology. Cell *168*, 657–669.

7. Weber, W.A. (2006). Positron emission tomography as an imaging biomarker. J. Clin. Oncol. *24*, 3282–3292.

8. Gallamini, A., Zwarthoed, C., and Borra, A. (2014). Positron emission tomography (PET) in oncology. Cancers *6*, 1821–1889.

9. Nair, V.S., Gevaert, O., Davidzon, G., Napel, S., Graves, E.E., Hoang, C.D., Shrager, J.B., Quon, A., Rubin, D.L., and Plevritis, S.K. (2012). Prognostic PET 18F-FDG uptake imaging features are associated with major oncogenomic alterations in patients with resected non–small cell lung cancer genomics of PET-FDG uptake in NSCLC. Cancer Res. *72*, 3725–3734.

10. Gatenby, R.A., Grove, O., and Gillies, R.J. (2013). Quantitative imaging in cancer evolution and ecology. Radiology *269*, 8–15.

11. O'Connor, J.P.B., Rose, C.J., Waterton, J.C., Carano, R.A.D., Parker, G.J.M., and Jackson, A. (2015). Imaging intratumor heterogeneity: role in therapy response, resistance, and clinical outcome. Clin. Cancer Res. *21*, 249–257.

12. O'Connor, J.P.B., Aboagye, E.O., Adams, J.E., Aerts, H.J.W.L., Barrington, S.F., Beer, A.J., Boellaard, R., Bohndiek, S.E., Brady, M., Brown, G., et al. (2017). Imaging biomarker roadmap for cancer studies. Nat. Rev. Clin. Oncol. *14*, 169–186.

13. Chihara, D., Oki, Y., Onoda, H., Taji, H., Yamamoto, K., Tamaki, T., and Morishima, Y. (2011). High maximum standard uptake value (SUVmax) on PET scan is associated with shorter survival in patients with diffuse large B cell lymphoma. Int. J. Hematol. *93*, 502–508.

14. Cima, S., Perrone, A.M., Castellucci, P., Macchia, G., Buwenge, M., Cammelli, S., Cilla, S., Ferioli, M., Ferrandina, G., Galuppi, A., et al. (2018). Prognostic impact of pretreatment fluorodeoxyglucose positron emission tomography/computed tomography SUVmax in patients with locally advanced cervical cancer. Int. J. Gynecol. Cancer *28*, 575–580.

15. Diao, W., Tian, F., and Jia, Z. (2018). The prognostic value of SUVmax measuring on primary lesion and ALN by 18F-FDG PET or PET/CT in patients with breast cancer. Eur. J. Radiol. *105*, 1–7.

16. Cheng, N.-M., Hsieh, C.-E., Liao, C.-T., Ng, S.-H., Wang, H.-M., Fang, Y.-H.D., Chou, W.-C., Lin, C.-Y., and Yen, T.-C. (2019). Prognostic value of tumor heterogeneity and SUVmax of pretreatment 18F-FDG PET/CT for salivary gland carcinoma with high-risk histology. Clin. Nucl. Med. *44*, 351–358.

17. Hicks, R.J. (2022). The value of the standardized uptake value (SUV) and metabolic tumor volume (MTV) in lung cancer. Semin. Nucl. Med. *52*, 734–744. https://doi.org/10.1053/j.semnuclmed.2022.04.007.

18. Beerenwinkel, N., Schwarz, R.F., Gerstung, M., and Markowetz, F. (2015). Cancer evolution: mathematical models and computational inference. Syst. Biol. *64*, e1–e25.

19. Bozic, I., and Wu, C.J. (2020). Delineating the evolutionary dynamics of cancer from theory to reality. Nat. Cancer *1*, 580–588.

20. Laughney, A.M., Elizalde, S., Genovese, G., and Bakhoum, S.F. (2015). Dynamics of tumor heterogeneity derived from clonal karyotypic evolution. Cell Rep. *12*, 809–820.

21. Lorenzi, T., Chisholm, R.H., Desvillettes, L., and Hughes, B.D. (2015). Dissecting the dynamics of epigenetic changes in phenotype-structured populations exposed to fluctuating environments. J. Theor. Biol. *386*, 166–176.

22. Bozic, I., Antal, T., Ohtsuki, H., Carter, H., Kim, D., Chen, S., Karchin, R., Kinzler, K.W., Vogelstein, B., and Nowak, M.A. (2010). Accumulation of driver and passenger mutations during tumor progression. Proc. Natl. Acad. Sci. USA 107, 18545–18550.

23. Jiménez-Sánchez, J., Bosque, J.J., Jiménez Londoño, G.A., Molina-García, D., Martínez, Á., Pérez-Beteta, J., Ortega-Sabater, C., Honguero Martínez, A.F., García Vicente, A.M., Calvo, G.F., and Pérez-García, V.M. (2021). Evolutionary dynamics at the tumor edge reveal metabolic imaging biomarkers. Proc. Natl. Acad. Sci. USA 118. e2018110118.

24. Hatton, I.A., Dobson, A.P., Storch, D., Galbraith, E.D., and Loreau, M. (2019). Linking scaling laws across eukaryotes. Proc. Natl. Acad. Sci. USA 116, 21616–21622.

25. Lee, E.D., Kempes, C.P., and West, G.B. (2021). Growth, death, and resource competition in sessile organisms. Proc. Natl. Acad. Sci. USA 118. e2020424118.

26. Pérez-García, V.M., Calvo, G.F., Bosque, J.J., León-Triana, O., Jiménez, J., Pérez-Beteta, J., Belmonte-Beitia, J., Valiente, M., Zhu, L., García-Gómez, P., et al. (2020). Universal scaling laws rule explosive growth in human cancers. Nat. Phys. 16, 1232–1237.

27. Steele, C.D., Abbasi, A., Islam, S.M.A., Bowes, A.L., Khandekar, A., Haase, K., Hames-Fathi, S., Ajayi, D., Verfaillie, A., Dhami, P., et al. (2022). Signatures of copy number alterations in human cancer. Nature 606, 984–991.

28. Vogelstein, B., and Kinzler, K.W. (2004). Cancer genes and the pathways they control. Nat. Med. 10, 789–799.

29. Lipinski, K.A., Barber, L.J., Davies, M.N., Ashenden, M., Sottoriva, A., and Gerlinger, M. (2016). Cancer evolution and the limits of predictability in precision cancer medicine. Trends Cancer 2, 49–63.

30. Greaves, M., and Maley, C.C. (2012). Clonal evolution in cancer. Nature 481, 306–313.

31. Cantor, J.R., and Sabatini, D.M. (2012). Cancer cell metabolism: one hallmark, many faces. Cancer Discov. 2, 881–898.

32. Lee, Y.-Y., Choi, C.H., Kim, C.J., Kang, H., Kim, T.-J., Lee, J.-W., Lee, J.-H., Bae, D.-S., and Kim, B.-G. (2009). The prognostic significance of the SUVmax (maximum standardized uptake value for F-18 fluorodeoxyglucose) of the cervical tumor in PET imaging for early cervical cancer: preliminary results. Gynecol. Oncol. 115, 65–68.

33. Berghmans, T., Dusart, M., Paesmans, M., Hossein-Foucher, C., Buvat, I., Castaigne, C., Scherpereel, A., Mascaux, C., Moreau, M., Roelandts, M., et al. (2008). Primary tumor standardized uptake value (SUVmax) measured on fluorodeoxyglucose positron emission tomography (FDG-PET) is of prognostic value for survival in non-small cell lung cancer (NSCLC): a systematic review and meta-analysis (MA) by the European Lung Cancer Working Party for the IASLC Lung Cancer Staging Project. J. Thorac. Oncol. 3, 6–12.

34. Varn, F.S., Johnson, K.C., Martinek, J., Huse, J.T., Nasrallah, M.P., Wesseling, P., Cooper, L.A.D., Malta, T.M., Wade, T.E., Sabedot, T.S., et al. (2022). Glioma progression is shaped by genetic evolution and microenvironment interactions. Cell 185, 2184–2199.e16.

35. Calabria, F.F., Barbarisi, M., Gangemi, V., Grillea, G., and Cascini, G.L. (2018). Molecular imaging of brain tumors with radiolabeled choline PET. Neurosurg. Rev. 41, 67–76.

36. Shields, A.F., Grierson, J.R., Dohmen, B.M., Machulla, H.J., Stayanoff, J.C., Lawhorn-Crews, J.M., Obradovich, J.E., Muzik, O., and Mangner, T.J. (1998). Imaging proliferation in vivo with [F-18] FLT and positron emission tomography. Nat. Med. 4, 1334–1336.

37. Vander Heiden, M.G., Cantley, L.C., and Thompson, C.B. (2009). Understanding the Warburg effect: the metabolic requirements of cell proliferation. Science 324, 1029–1033.

38. Pikor, L., Thu, K., Vucic, E., and Lam, W. (2013). The detection and implication of genome instability in cancer. Cancer Metastasis Rev. 32, 341–352.

39. Drews, R.M., Hernando, B., Tarabichi, M., Haase, K., Lesluyes, T., Smith, P.S., Morrill Gavarró, L., Couturier, D.-L., Liu, L., Schneider, M., et al. (2022). A pan-cancer compendium of chromosomal instability. Nature 606, 976–983.

40. Sansregret, L., Vanhaesebroeck, B., and Swanton, C. (2018). Determinants and clinical implications of chromosomal instability in cancer. Nat. Rev. Clin. Oncol. 15, 139–150.

41. Bakhoum, S.F., and Compton, D.A. (2012). Chromosomal instability and cancer: a complex relationship with therapeutic potential. J. Clin. Invest. 122, 1138–1143.

42. Giam, M., and Rancati, G. (2015). Aneuploidy and chromosomal instability in cancer: a jackpot to chaos. Cell Div. 10, 3–12.

43. Marine, J.-C., Dawson, S.-J., and Dawson, M.A. (2020). Non-genetic mechanisms of therapeutic resistance in cancer. Nat. Rev. Cancer 20, 743–756.

44. Fennell, K.A., Vassiliadis, D., Lam, E.Y.N., Martelotto, L.G., Balic, J.J., Hollizeck, S., Weber, T.S., Semple, T., Wang, Q., Miles, D.C., et al. (2022). Non-genetic determinants of malignant clonal fitness at single-cell resolution. Nature 601, 125–131.

45. Duncan, E.J., Gluckman, P.D., and Dearden, P.K. (2014). Epigenetics, plasticity, and evolution: how do we link epigenetic change to phenotype? J. Exp. Zool. B Mol. Dev. Evol. 322, 208–220.

46. Heide, T., Househam, J., Cresswell, G.D., Spiteri, I., Lynn, C., Mossner, M., Kimberley, C., Fernandez-Mateos, J., Chen, B., Zapata, L., et al. (2022). The co-evolution of the genome and epigenome in colorectal cancer. Nature 611, 733–743.

47. Landau, D.A., Clement, K., Ziller, M.J., Boyle, P., Fan, J., Gu, H., Stevenson, K., Sougnez, C., Wang, L., Li, S., et al. (2014). Locally disordered methylation forms the basis of intratumor methylome variation in chronic lymphocytic leukemia. Cancer Cell 26, 813–825.

48. Pillai, M., and Jolly, M.K. (2021). Systems-level network modeling deciphers the master regulators of phenotypic plasticity and heterogeneity in melanoma. iScience 24, 103111.

49. Eling, N., Morgan, M.D., and Marioni, J.C. (2019). Challenges in measuring and understanding biological noise. Nat. Rev. Genet. 20, 536–548.

50. Shaffer, S.M., Dunagin, M.C., Torborg, S.R., Torre, E.A., Emert, B., Krepler, C., Beqiri, M., Sproesser, K., Brafford, P.A., Xiao, M., et al. (2017). Rare cell variability and drug-induced reprogramming as a mode of cancer drug resistance. Nature 546, 431–435.

51. Cerulus, B., New, A.M., Pougach, K., and Verstrepen, K.J. (2016). Noise and epigenetic inheritance of single-cell division times influence population fitness. Curr. Biol. 26, 1138–1147.

52. Hashimoto, M., Nozoe, T., Nakaoka, H., Okura, R., Akiyoshi, S., Kaneko, K., Kussell, E., and Wakamoto, Y. (2016). Noise-driven growth rate gain in clonal cellular populations. Proc. Natl. Acad. Sci. USA 113, 3251–3256.

53. Lorenzi, T., Chisholm, R.H., and Clairambault, J. (2016). Tracking the evolution of cancer cell populations through the mathematical lens of phenotype-structured equations. Biol. Direct 11, 43.

54. Chisholm, R.H., Lorenzi, T., Desvillettes, L., and Hughes, B.D. (2016). Evolutionary dynamics of phenotype-structured populations: from individual-level mechanisms to population-level consequences. Z. Angew. Math. Phys. 67, 1–34.

55. Chisholm, R.H., Lorenzi, T., Lorz, A., Larsen, A.K., de Almeida, L.N., Escargueil, A., and Clairambault, J. (2015). Emergence of drug tolerance in cancer cell populations: an evolutionary outcome of selection, nongenetic instability, and stress-induced adaptation. Cancer Res. 75, 930–939.

56. Villa, C., Chaplain, M.A., and Lorenzi, T. (2021). Modeling the emergence of phenotypic heterogeneity in vascularized tumors. SIAM J. Appl. Math. 81, 434–453.

57. Ortega-Sabater, C., F Calvo, G., Dinić, J., Podolski, A., Pesic, M., and Pérez-García, V. (2023). Stochastic fluctuations drive non-genetic evolution of proliferation in clonal cancer cell populations. Bull. Math. Biol. 85, 8.

58. Mattingly, H.H., and Emonet, T. (2022). Collective behavior and nongenetic inheritance allow bacterial populations to adapt to changing environments. Proc. Natl. Acad. Sci. USA 119. e2117377119.

59. Narla, A.V., Cremer, J., and Hwa, T. (2021). A traveling-wave solution for bacterial chemotaxis with growth. Proc. Natl. Acad. Sci. USA *118*. e2105138118.

60. Rocha, H.L., Godet, I., Kurtoglu, F., Metzcar, J., Konstantinopoulos, K., Bhoyar, S., Gilkes, D.M., and Macklin, P. (2021). A persistent invasive phenotype in post-hypoxic tumor cells is revealed by fate mapping and computational modeling. iScience *24*, 102935.

61. Shelton, S.E., Nguyen, H.T., Barbie, D.A., and Kamm, R.D. (2021). Engineering approaches for studying immune-tumor cell interactions and immunotherapy. iScience *24*, 101985.

62. Clark, K., Vendt, B., Smith, K., Freymann, J., Kirby, J., Koppel, P., Moore, S., Phillips, S., Maffitt, D., Pringle, M., et al. (2013). The Cancer Imaging Archive (TCIA): maintaining and operating a public information repository. J. Digit. Imaging *26*, 1045–1057.

63. Vallieres, M., Kay-Rivest, E., Perrin, L.J., Liem, X., Furstoss, C., Aerts, H.J., Khaouam, N., Nguyen-Tan, P.F., Wang, C.-S., Sultanem, K., et al. (2017). Radiomics strategies for risk assessment of tumour failure in head-and-neck cancer. Sci. Rep. *7*, 1–14.

64. Kostakoglu, L., Duan, F., Idowu, M.O., Jolles, P.R., Bear, H.D., Muzi, M., Cormack, J., Muzi, J.P., Pryma, D.A., Specht, J.M., et al. (2015). A phase II study of 3'-deoxy-3'-18F-fluorothymidine PET in the assessment of early response of breast cancer to neoadjuvant chemotherapy: results from ACRIN 6688. J. Nucl. Med. *56*, 1681–1689.

65. Boellaard, R. (2009). Standards for PET image acquisition and quantitative data analysis. J. Nucl. Med. *50*, 11S–20S.

66. Schiesser, W.E. (2016). Method of Lines PDE Analysis in Biomedical Science and Engineering (John Wiley & Sons, Inc).

67. Jbabdi, S., Mandonnet, E., Duffau, H., Capelle, L., Swanson, K.R., Pélégrini-Issac, M., Guillevin, R., and Benali, H. (2005). Simulation of anisotropic growth of low-grade gliomas using diffusion tensor imaging. Magn. Reson. Med. *54*, 616–624.

68. Pérez-García, V.M., Calvo, G.F., Belmonte-Beitia, J., Diego, D., and Pérez-Romasanta, L. (2011). Bright solitary waves in malignant gliomas. Phys. Rev. E Stat. Nonlin. Soft Matter Phys. *84*, 021921.

69. Belmonte-Beitia, J., Calvo, G.F., and Pérez-García, V.M. (2014). Effective particle methods for Fisher–Kolmogorov equations: theory and applications to brain tumor dynamics. Commun. Nonlinear Sci. Numer. Simul. *19*, 3267–3283.

STAR★METHODS

KEY RESOURCES TABLE

REAGENT or RESOURCE	SOURCE	IDENTIFIER
Software and algorithms		
MATLAB (R2020a)	The MathWork, Inc. Natick, MA	https://www.mathworks.com/products/matlab.html

RESOURCE AVAILABILITY

Lead contact

Further information and requests for resources and reagents should be directed to and will be fulfilled by the Lead Contact, Jesús J. Bosque (jesus.bosque@uclm.es).

Materials availability

This study did not utilize any physical material.

Data and code availability

This paper does not report original code. Any additional information required to reanalyze the data reported in this paper is available from the lead contact upon request.

EXPERIMENTAL MODEL AND SUBJECT DETAILS

Lung cancer patients (LUAD & LUSC)

Lung cancer patients (LUAD & LUSC) were gathered from a multicenter prospective study of patients who underwent surgery between June 2007 and December 2016. The Institutional Review Boards (IRB) from the participating hospitals approved the study, and every patient signed a written informed consent. Only patients with a maximum longitudinal size in computed tomography scan (CT) larger than 2 cm were selected. 115 LUAD patients (92 men, 23 women, age range 48–81 years, median 65 years) were included in the dataset, of which 3 were excluded due to complications of surgery leading to the death of the patient, 4 were discarded for having metastases present at diagnosis, and 2 were omitted due to the lack of clinical data. The data from PET images of the remaining 106 patients were used in this study. The distribution of stages was: 44 stage I, 36 stage II, 26 stage III, and 0 stage IV (due to exclusion). The TNM staging was: 23 T1, 67 T2, 14 T3, and 2 T4; 69 N0, 16 N1, 21 N2; all M0. 139 LUSC patients were collected (122 men, 17 women, age range 47–78 years, median 64 years). Of them, 5 patients were excluded due to post-surgery death and 3 were discarded due to the presence of metastasis at the time of diagnosis. Criteria and protocol were as in the LUAD group. Staging was: 47 stage I, 45 stage II, and 39 stage II. TNM staging was: 27 T1, 64 T2, 25 T3, and 15 T4; 84 N0, 27 N1, 20 N2; 131 M0. The PET machine was a dedicated whole-body PET/CT scanner (Discovery SDTE-16s; GE Medical Systems) in three-dimensional (3D) mode. Image acquisition began 60 min after intravenous administration of approximately 370 MBq (10 mCi) of ^{18}F-FDG; the images obtained had a voxel size of 5.47×5.47×3.27 mm, with no gap between slices, and a matrix size of 128 × 128. The inclusion criteria considered only newly diagnosed patients with available pretreatment PET/CT examination and a lesion uptake higher than background (SUV_{max} larger than twice the background), and absence of distant metastases.

Breast cancer patients (BC)

61 patients (all women, age range 25–80 years, median 51 years) from a multicenter prospective study, beginning in September 2009, were included in the study. The study was approved by the IRB of Hospital General Universitario de Ciudad Real, Spain. Written informed consent was obtained from all the patients. Histologies were 59 ductal carcinomas and 2 lobular carcinomas. The following inclusion criteria were used: (1) newly diagnosed locally advanced breast cancer with clinical indication of neoadjuvant chemotherapy, (2) lesion uptake in PET images higher than background, (3) absence of distant metastases, and (4) tumor size bigger than 2 cm. The protocol, procedure, and PET/CT machine were as in the LUAD group. 15 patients had N0, 35 N1, 4 N2, and 7 N3. PET machine and protocol was as in the case of lung cancer patients.

Head and neck cancer patients (HNC)

PET images were acquired from the The Cancer Imaging Archive (TCIA)[62] and the Head-Neck-PET-CT collection (H&N1 dataset).[63] This cohort was composed of 92 patients with primary squamous cell carcinoma of the head and neck (stages I-IV) treated between 2006 and 2014 at Hôpital Général Juif (Montreal, Canada). The inclusion criteria in the present study were: (1) availability of pretreatment PET studies and (2) presence of a well-defined primary tumor. 76 patients (63 men, 13 women, age range 18–84 years, median 62 years) were selected satisfying these criteria. The locations of the tumor were: 3 hypopharynges, 13 larynges, 11 nasopharynges and 49 oropharynges. The staging was: 0 stage I, 4 stage II, 26 stage III, and 46 stage IV. The TNM staging distribution was: 11 T1, 19 T2, 34 T3, and 12 T4; 11 N0, 16 N1, 47 N2, and 2 N3; 72 M0 and 4 Mx. FDG-PET scans were obtained from a hybrid PET/CT scanner (Discovery ST, GE Healthcare) within 37 days before treatment (median: 14 days). A median of 584 MBq (range: 368–715) was injected intravenously. Imaging acquisition of the head and neck was performed using multiple bed positions with a median of 300 s (range: 180–420) per bed position. The slice thickness resolution was 3.27 mm for all patients and the median in-plane resolution was 3.52×3.52 mm (range: 3.52–4.69).

Breast cancer patients (BC-FLT)

This cohort included pretreatment ^{18}F-FLT PET/CT scans of patients from the American College of Radiology Imaging Network (ACRIN) 6688 study. This study was observational, non-randomized, multicenter phase II and the data are available at the TCIA (ACRIN-FLT-Breast).[64] This dataset included histologically confirmed breast cancer patients with the following inclusion criteria: (i) primary breast cancer measuring 2 cm or more (ii) candidate for neoadjuvant chemotherapy (NAC) and surgical resection of the residual primary tumor after chemotherapy, and (iii) no distant metastases present. All patients received a baseline pretreatment ^{18}F-FLT PET/CT study within 4 weeks before NAC initiation. After the injection of 2.6 MBq/kg (mean, 167 MBq; range, 110–204 MBq), a whole-body image (5–7 bed positions) was obtained at 60 min (mean, 70 min; range, 50–101 min). All patients were scanned on calibrated and ACRIN-accredited PET/CT scanners, which incorporated a review of image quality and testing of SUVs using a uniform phantom and review of images. 78 patients were included in the study (100% women, age range 22–83 years, median 50 years).

Glioma patients (GLI)

Patients with informed consent were included consecutively from a prospective non-randomized multicenter study approved by the IRB of the participating hospitals (FuMeGA: Functional and Metabolic Glioma Analysis). A basal ^{18}F-fluorocholine PET/CT scan was performed in glioma patients after MRI with an operable brain lesion and a good performance status (ECOG ≤ 2). Only patients with pathologically confirmed brain glioma were included. Our study comprised 65 patients from the period 2017–2019 of which 5 were excluded. The histologies of the 60 remaining patients (39 men, 21 women, age range 23–80 years, median 64 years) were 51 glioblastomas (3 of them IDH mutant), 8 anaplastic astrocytomas, and 1 oligodendroglioma. The same hybrid equipment (Discovery DSTXL-1, General Electric) was used for all the PET/CT scans. 185 MBq of ^{18}F-FCHOL were administered intravenously and PET registration was initiated 40 min afterward. First, a brain scan was performed starting with a low-dose CT transmission study (modulated 120 kV and 80 mA) without intravenous contrast, followed by a 3D emission study with an acquisition time of 20 min (one single bed). Voxel size was 2.34×2.34×3.27 mm.

METHOD DETAILS
PET image analysis

An experienced nuclear medicine physician (A.M.G.V.) and an imaging engineer (J.P.-B.) independently assessed the PET scans in an Advantage Windows station (v.4.). PET scans were considered positive if SUV$_{max}$ was higher than twice the uptake of the normal tissue background. Only positive PET scans were considered for subsequent tumor segmentation. PET images in DICOM (Digital Imaging and Communication in Medicine) files were imported into the scientific software package MATLAB (R2020a, The MathWorks, Inc., Natick, MA, USA). The tumor was first manually located in a 3D box and then delineated by an expert (A.M.G.V., J.P.-B., V.M.P.-G., and J.J.B.) with the aid of a guiding semiautomatic algorithm. All segmentations were performed using an in-house developed software that allowed the support of a digital pencil on a tablet. Physiological activity contiguous with tumor uptake, e.g. choroid plexus or skull in the brain, was manually excluded from the tumor segmentations. From the radiotracer concentration in each voxel, the radiotracer SUV is given by

$$SUV = \frac{ACvox}{FDGdose/W},$$ (Equation 2)

where ACvox represents the average activity concentration in a voxel in kBq/mL, FDGdose is the dose of the radiotracer administered in MBq and W is the body weight in kg.[65] The DICOM files contain a stored value S_v that has to be scaled by the slope R_S to retrieve the actual concentration in a voxel ACvox $= S_v \cdot R_S$. Moreover, the radiation dose FDGdose is subjected to natural exponential decay so the injected total dose R_{TD} has to be corrected for the time that it takes from injection to the specific voxel to be processed (E_t). This implies an additional term $D_F \cdot e^{\ln(2)E_t/H_F}$, with D_F the decay factor of the radiopharmaceutical and H_F its half-life. Altogether, this leads to the formula from which SUV was computed

$$SUV = \frac{S_v \times R_S \times W}{R_{TD} \times D_F \times e^{\ln(2)E_t/H_F}}.$$ (Equation 3)

Global metabolic parameters were computed from the segmented images using the MATLAB software. The results of the delineation procedure gave rise to a 3D matrix containing the SUV values (S_i) of the N voxels of the tumor. For every tumor we calculated the following metrics:

- **MTV:** Metabolic tumor volume, corresponding to the volume of the segmented region, computed as the number N of selected voxels multiplied by the volume of one voxel V_V

$$MTV = N \times V_V.$$ (Equation 4)

- **TLA:** Total lesion activity (corresponding to total lesion glycolysis, TLG, in the groups where ^{18}F-FDG was used), calculated as the sum of the SUV value multiplied by the volume of the voxel for all the N voxels in the tumor

$$TLA = \sum_{i=1}^{N} S_i \times V_V.$$ (Equation 5)

- **SUV$_{max}$:** Maximum value of SUV in the tumor

$$SUV_{max} = \max\{S_i : i = 1, 2, \ldots, N\}.$$ (Equation 6)

- **SUV$_{mean}$:** Average value of SUV in the tumor calculated as the quotient

$$SUV_{mean} = \frac{TLA}{MTV}.$$ (Equation 7)

Scaling laws

For each cohort, scaling laws for variables Y versus X were obtained by log-plotting Y versus X and fitting the datasets to a power law of the form

$$Y = \alpha X^{\beta},$$ (Equation 8)

where α is a (positive) rate constant, and β is the scaling exponent. The value of the exponent β has important implications for the behavior of the system and distinguishes between sublinear ($\beta < 1$) and superlinear ($\beta > 1$) scalings. In turn, α is just a constant of proportionality with little implications; for the sake of clarity, its value is not stated along the manuscript, even though it is calculated for the different fits presented here.

Numerical solution of the PDE model

We simulated the growth of the tumor using Equation 1 assuming a spherical geometry $\Omega = [0, R_{\mathrm{lim}}]$, with R_{lim} denoting the maximum radius of the computational window, which was set at $R_{\mathrm{lim}} = 6$ cm. The PDE reads then as

$$\frac{\partial u}{\partial t} = D_c \left(\frac{\partial^2 u}{\partial r^2} + \frac{2}{r} \frac{\partial u}{\partial r} \right) + D_\rho \frac{\partial^2 u}{\partial \rho^2} + (\rho - \mu) \left(1 - \frac{1}{K} \int_0^{\rho_m} u(r, \rho', t) d\rho' \right) u(r, \rho, t), \qquad \text{(Equation 9)}$$

where $r \geq 0$ denotes the radial distance from the tumor center. The initial condition for Equation 9 was taken to be

$$u(r, \rho, 0) = u_0 \exp \left(- \frac{r^2}{2\sigma_r^2} - \frac{(\rho - \rho_0)^2}{2\sigma_\rho^2} \right), \qquad \text{(Equation 10)}$$

where u_0 and σ_r denote the amplitude and the SD of the spatial profile, respectively. Parameters were set to $u_0 = 3.4 \times 10^9$ cell day cm^{-3}, $\sigma_r = 0.07$ cm, $\rho_0 = 2.2 \times 10^{-2}$ day^{-1}, and $\sigma_\rho = 2 \times 10^{-3}$ day^{-1}.

Homogeneous Neumann boundary conditions were imposed at $r = 0$ and $r = R_{\mathrm{lim}}$. Equation 9, in the non-normalised form showed, was solved numerically by means of the method of lines.[66] The computational domain, (r, ρ), chosen as $[0, 6]$cm $\times [0, 0.06]$day^{-1}, was discretised in a mesh consisting of 401×241 equi-spaced nodes. The parameters representing the characteristics of the cell population and evolutionary dynamics, which were included explicitly in the computation, were $D_c = 1.3 \times 10^{-4}$ cm^2 day^{-1}, $D_\rho = 1.6 \times 10^{-8}$ day^{-3}, $\mu = 4.0 \times 10^{-3}$ day^{-1}, and $K = 6.0 \times 10^7$ cell cm^{-3}. D_c was taken from previous publications.[67–69] The parameter modulating the death rate μ is equivalent to an estimated half-life of 250 days, and the carrying capacity was estimated from a maximum packing of cells *in vivo* corresponding to a cube of 23 µm^3 side. The value of the variability of phenotypes D_ρ cannot be retrieved from the literature, since for the moment there are no available experiments that quantify it, and therefore we used values for which our results resembled the data from patients (see discussion section). Since the EvoFK equation is non-local, the method of lines was adapted to include numerical integration using Simpson's rule for quadratures. This led to a system of coupled ordinary differential equations (ODEs) in time for each point in the space/pheno-type computational window. The resulting ODE system was solved using the stiff MATLAB (R2020a, The MathWorks, Inc., Natick, MA, USA) solver `ode15s`.

Definition of the key quantities from the model

From the solution $u(\mathbf{x}, \rho, t)$ of Equation 1, a number of useful quantities can be calculated:

- **Marginal cell density:** Number of tumor cells at point $\mathbf{x}$ and time t,

$$n(\mathbf{x}, t) = \int_0^{\rho_m} u(\mathbf{x}, \rho, t) \, d\rho, \qquad \text{(Equation 11)}$$

where ρ_m denotes the maximum (biologically feasible) proliferation rate.

- **Proliferation activity:** Density of tumor cells produced at point $\mathbf{x}$ and time t due to mitosis

$$\mathcal{A}(\mathbf{x}, t) = \int_0^{\rho_m} \rho \left(1 - \frac{1}{K} \int_0^{\rho_m} u(\mathbf{x}, \rho', t) d\rho' \right) u(\mathbf{x}, \rho, t) d\rho. \qquad \text{(Equation 12)}$$

- **Probability distribution of proliferation rates:** Fraction of tumor cells that have a proliferation rate ρ at a time t over the total number of cells

$$P(\rho, t) = \frac{\int_\Omega u(\mathbf{x}, \rho, t) d\mathbf{x}}{\int_0^{\rho_m} \int_\Omega u(\mathbf{x}, \rho, t) d\mathbf{x} \, d\rho}. \qquad \text{(Equation 13)}$$

- Local averaged proliferation rate:

$$\overline{\rho}(\mathbf{x}, t) \ = \ \frac{\int_0^{\rho_m} u(\mathbf{x}, \rho, t)\rho \, d\rho}{n(\mathbf{x}, t)}. \qquad \text{(Equation 14)}$$

- Metabolic tumor volume (*in silico*): We replicated the process used in the PET images. To do so, we selected a proliferation activity threshold $\mathcal{A}_{\text{th}}$, set in our case to $\mathcal{A}_{\text{th}} = 8500$ cell cm^{-3} day^{-1}, and considered only those regions with a higher activity $\mathcal{A} > \mathcal{A}_{\text{th}}$. Then, we performed the following spatial integration over that domain $\Omega_{\text{th}} : \ = \ \{\mathbf{x} \in \Omega | \mathcal{A}(t) > \mathcal{A}_{th}\}$

$$\text{MTV}(t) \ = \ \int_{\Omega_{\text{th}}} d\mathbf{x}. \qquad \text{(Equation 15)}$$

- Total lesion activity (*in silico*): The calculation of the total activity in the simulated tumor emulated the procedure applied to medical PET images taking only the regions with $\mathcal{A} > \mathcal{A}_{\text{th}}$ and integrating over the computational domain $\Omega_{\text{th}} : \ = \ \{\mathbf{x} \in \Omega | \mathcal{A}(t) > \mathcal{A}_{th}\}$

$$\text{TLA}(t) \ = \ \int_{\Omega_{\text{th}}} \mathcal{A}(\mathbf{x}, t) d\mathbf{x}. \qquad \text{(Equation 16)}$$

- Maximum proliferation activity: The maximum of the profile of proliferation activity was evaluated similarly to the case of the images as

$$\mathcal{A}_{\text{max}}(t) \ = \ \max_{\mathbf{x} \in \Omega} \mathcal{A}(\mathbf{x}, t). \qquad \text{(Equation 17)}$$

- Mean proliferation activity: The mean activity was computed as the ratio between the total lesion activity and the metabolic tumor volume of the *in silico* tumor

$$\mathcal{A}_{\text{mean}}(t) \ = \ \frac{\text{TLA}(t)}{\text{MTV}(t)}. \qquad \text{(Equation 18)}$$

All the above integrals were calculated by means of Simpson's rule for numerical quadrature.

Generation of synthetic patient cohorts

We run simulations of Equation 9 for a group of 150 virtual patients with parameters randomly chosen in the ranges $D_c \in [1 \times 10^{-4}, 1.5 \times 10^{-4}]$ cm^2 day^{-1}, $D_\rho \in [2.5 \times 10^{-9}, 4 \times 10^{-8}]$ day^{-3}, $\mu \in [1 \times 10^{-3}, 5 \times 10^{-3}]$ day^{-1} using uniform distributions. The value of the carrying capacity K, which was not expected to show high inter patient variability, was fixed to $K = 6.0 \times 10^7$ cell cm^{-3}.

The proliferation-space mesh (r, ρ) was discretized using 351×181 equispaced nodes. The initial conditions were taken as in Equation 10, taking parameters randomly in the ranges $\rho_0 \in [2 \times 10^{-2}, 2.4 \times 10^{-2}]$ day^{-1} and $\sigma_\rho \in [7 \times 10^{-4}, 4.5 \times 10^{-3}]$ day^{-1}. The endpoint of the simulation was drawn from an uniform distribution $t_{\text{diag}} \in [500, 1000]$ day. The endpoint of the simulations was considered to correspond to the patient initial

PET imaging study at diagnosis time. The variables MTV, TLA, $\mathcal{A}_{max}$ and $\mathcal{A}_{mean}$ were calculated at these final times t_{diag} for each simulation. Additionally, we performed a sensitivity analysis of these results by carrying out 1650 more simulations. This sensitivity analysis was performed in four groups of simulations fixing one parameter at a time in different values while the others were randomly chosen in the said ranges. We performed this analysis for three fixed values of D_c, three fixed values of D_p, two fixed values of K (besides the already fixed value used for the definite simulations in the results section), and three fixed values of μ. In this way, we generated eleven more groups of *in silico* patients which confirm the validity of the model for different values of the parameters.

QUANTIFICATION AND STATISTICAL ANALYSIS

Statistical analysis of power law regressions and Spearman's rank correlation

As a previous examination of the relationships existing in the data, we computed the Spearman's rank correlation coefficient r_s between pairs of variables. This statistic assesses how well the relationship between two variables is described by a monotonic function, what is evaluated by analyzing the ranks of the pairs of data. The sign indicates the direction of the association between variables: positive when both variables tend to increase together, and negative otherwise. A perfect correspondence in the ranks of the pairs of data will yield a r_s equal to $+1$ or -1, while $r_s = 0$ indicates no relationship between the variables. Spearman's rank correlation coefficient is the same as the Pearson correlation coefficient between the rank variables. The calculations of the Spearman's rank correlation coefficients were made through the function `corr` of the same MATLAB (R2020a, The MathWorks, Inc., Natick, MA, USA).

After the initial evaluation by the Spearman's rank correlation coefficient, we performed a fit of the pairs of data to power laws of the form Equation 8. All the regressions to power laws carried out in this article were performed as linear least squares fits (with two parameters) of the logarithmic transformed variables. The fit and the associated statistics were computed through the `fitlm` function of MATLAB (R2020a, The MathWorks, Inc., Natick, MA, USA). The goodness of fit was determined by the coefficient of determination R^2, which gives the proportion of the variation in the dependent variable that is explained by the statistical model (in this case, a linear regression). In a set of data Y_i with mean $\overline{Y}$ which is fit by f_i, the coefficient of determination is given by

$$R^2 = 1 - \frac{\sum_i (Y_i - f_i)^2}{\sum_i (Y_i - \overline{Y})^2}.$$

(Equation 19)

Values of R^2 closer to 1 indicate a better fit of the statistical model to the data, while low values close to 0 indicate that the variability of the data is badly predicted by the regression.